



**Numerical modelling of ENAs
from stellar wind interactions**

ANDREAS EKENBÄCK

Doctoral Thesis
Kiruna, Sweden 2008

IRF Scientific Report 297
ISSN 0284-1703
ISBN 978-91-977255-5-2

Swedish Institute of Space Physics
P.O. Box 812
SE-981 28 Kiruna
SWEDEN

Akademisk avhandling som med tillstånd av rektorsämbetet vid Umeå universitet fram-
lägges till offentlig granskning för avläggande av teknologie doktorsexamen i rymdteknik
fredagen den 26 september 2008 klockan 10.00 i Aulan, Institutet för rymdfysik, Etian 100,
Kiruna.

© Andreas Ekenbäck, augusti 2008

Tryck: Universitetsservice US AB

Abstract

Energetic neutral atoms (ENAs) are produced whenever a stellar wind encounters a neutral atmosphere. If a stellar wind proton comes sufficiently close to a neutral a charge-exchange reaction may take place, transforming the proton into an ENA. Unaffected by magnetic and electric fields, ENAs provide an opportunity for global imaging of stellar wind interactions.

This thesis presents methods and results of numerical modelling of stellar wind interactions. In particular it treats in depth production of ENAs at comets, Mars and the extrasolar planet HD 209458b.

Sufficiently accurate numerical models of stellar wind interactions require extensive computations. Parallel computing has therefore been used throughout the work, both for fluid and particle simulations of space plasmas. This thesis describes the use of a general simulation tool, providing parallel computing for space plasma simulations.

The thesis presents estimations of the magnitude and morphology of the ENA production at comets and HD 209458b. It compares the results obtained with observations and analyzes them in the light of ENA production at similar objects. Also, simulated ENA images for Mars were produced and compared to observations.

Sammanfattning

Energirika neutrala atomer (ENA) bildas när en stjärnvind möter en neutral atmosfär. Om en stjärnvindsproton kommer tillräckligt nära en neutral så uppstår ett laddningsutbyte och protonen blir en ENA. ENA färdas opåverkade av magnetiska och elektriska fält och utgör en möjlighet för globala studier av stjärnvindsväxelverkan.

Den här avhandlingen presenterar metoder och resultat för numeriska modeller av stjärnvindsväxelverkan. Den behandlar specifikt produktion av ENA vid kometer, Mars och exoplaneten HD 209458b.

Tillräckligt noggranna numeriska modeller kräver omfattande beräkningar. Parallella beräkningar har därför använts genomgående, både för vätske- och partikelsimuleringar av rymdplasma. Avhandlingen beskriver användning av ett generellt simuleringsverktyg för rymdfysik och tillhandahåller därigenom en metod för parallella simuleringar av rymdplasma.

Avhandlingen presenterar en uppskattning av storleksordningen och morfologin av ENA-produktionen vid kometer och HD 209458b. Erhållna resultat jämförs med observationer och analyseras med utgångspunkt i ENA-produktion vid liknande objekt. Dessutom presenteras ENA-bilder av Mars och jämförs med observationer.

Contents

Contents	v
List of included papers	1
1 Introduction	3
1.1 Numerical modelling as experiments	3
1.2 Numerical modelling as a complement to observations	3
1.3 Notation	4
2 Stellar wind interactions	5
2.1 The solar wind	5
2.2 Comets	5
2.3 Mars	8
2.4 Exoplanets and the significance of HD 209458b	10
3 Energetic neutral atoms	13
3.1 ENA theory	13
3.2 Simulating ENA images	14
4 Numerical models for space plasmas	17
4.1 Fluid models	17
4.2 Particle models	21
4.3 Kinetic theory	22
4.4 Hybrid models	22
5 High Performance Computing	23
5.1 Parallel computing	23
5.2 The FLASH code	26
6 Summary of included papers	29
Bibliography	33

List of included papers

This thesis is based on the following papers, which are referred to in the text by their Roman numerals.

- I Ekenbäck, A., Holmström, M., Wurz, P., Griesmeier, J.-M., Lammer, H., Selsis, F. & Penz, T. Energetic neutral atoms around HD 209458b: Estimations of magnetospheric properties. *Astrophysical Journal*, 2008. *Submitted*
- II Galli, A., Wurz, P., Kallio, E., Ekenbäck, A., Holmström, M., Barabash, S., Grigoriev, A., Futaana, Y., Fok, M.C. & Gunell, H. The tailward flow of energetic neutral atoms observed at Mars. *Journal of Geophysical Research*, 2008. *Submitted*
- III Ekenbäck, A., Holmström, M., Barabash, S. & Gunell, H. Energetic neutral atom imaging of comets. *Geophysical Research Letters*, **35** (L05103), 2008.
- IV Holmström, M., Ekenbäck, A., Selsis, F., Penz, T., Lammer, H. & Wurz, P. Energetic neutral atoms as the explanation for the high-velocity hydrogen around HD 209458b. *Nature*, **451**, 970–972, 2008.
- V Ekenbäck, A. & Holmström, M. MHD modeling of the interaction between the solar wind and solar system objects. In Dongarra, J., Madsen, K. & Wasniewski, J. (eds.), *Proceedings of PARA'04 State-of-the-Art*, volume 3732 of *Lecture Notes in Computer Science*, pp. 554–562. Springer-Verlag, Berlin, Germany, 2006.

Reprints were made with permission from the publishers.

Other papers by the author

- Galli, A., Fok, M., Wurz, P., Barabash, S., Grigoriev, A., Futaana, Y., Holmström, M., Ekenbäck, A. *et al.* The tailward flow of energetic neutral atoms observed at Venus. *Journal of Geophysical Research*, 2008. *Accepted*
- Westerberg, L. G., Vedin, J., Ekenbäck, A. & Åkerstedt, H. O. Three-dimensional flow near a reconnection site at the dayside magnetopause: Analytical solutions coupled with MHD simulations. *Journal of Plasma Physics*, **73**, 811–819, 2007.
- Brinkfeldt, K., Gunell, H., Brandt, P., Barabash, S., Frahm, R., Winningham, J., Kallio, E., Holmström, M., Futaana, Y., Ekenbäck, A. *et al.* First ENA observations at Mars: Solar-wind ENAs on the nightside. *Icarus*, **182**, 439–447, 2006.
- Gunell, H., Brinkfeldt, K., Holmström, M., Brandt, P., Barabash, S., Kallio, E., Ekenbäck, A. *et al.* First ENA observations at Mars: Charge exchange ENAs produced in the magnetosheath. *Icarus*, **182**, 431–438, 2006.

Introduction

Numerical models and tests play an important part in many scientific fields. They can be used as standalone experiments as well as a complement to observations. Numerical modelling plays an especially important part in both space physics and astrophysics because of the special nature of these fields. Observations are expensive and rare, not to mention the difficulties associated with the space environment. Missions therefore have to be carefully planned—what instruments should we send up, to where and what should they study—and observations must often be compared to what we, with the current models, expect to see. Large savings of time and money are possible whenever numerical modelling can replace instrumentation.

Another important aspect that underlines the importance of numerical modelling is that space experiments are of an observational nature, and we cannot control the conditions of the system under study. Reproducing a system's behaviour, and measurements thereof, in numerical tests is therefore critical to identify laws governing the system.

1.1 Numerical modelling as experiments

For a large number of physical processes direct observations might be impossible. One example is the formation of our solar system or any other physical process that is difficult to recreate. Numerical modelling is essential to test, confirm and develop theories in these scientific areas.

For other phenomena, observations might be limited in time and/or space. Numerical modelling can be used to study these phenomena under different conditions. An example is the study of Mars, for which the observational possibilities are rare compared to the urge for knowledge.

There is also a vast number of phenomena for which we currently have a limited understanding of the processes and/or quantities. For such phenomena numerical modelling can be used to test hypotheses. An example of such usage of numerical modelling is presented in Paper IV where numerical simulations show how observational data from an object, for which our knowledge is limited, could be explained.

1.2 Numerical modelling as a complement to observations

Numerical modelling can be used ahead of experiments to improve the design of instruments and to plan the experimental agenda. An example of such numerical modelling is presented in Paper III which shows the possibility to study comets with similar instrumentation as already used at several planets. The results of Paper III were also used to plan the

operations of the available detectors in orbit around Venus to maximize the possibility of detecting comet 45P/Honda-Mrkos-Pajdusakova.

Physical experiments have for a long time been the only available tool for measurements. During a first stage in the data analysis of experiments we often need to interpret data by studying what we would expect given the physical models at hand. Numerical modelling can often be a helpful tool in such situations. Example of numerical modelling for that purpose is presented in Paper II where a study is done to see if existing models can explain the observations on the nightside of Mars.

1.3 Notation

In what follows we use SI units as far as possible. Vectors are denoted by bold symbols, and the corresponding normal symbol is used for the magnitude of the vector. The corresponding symbol with a subscript denotes a component of the vector. The following symbols are used throughout the thesis:

B	magnetic field
c	speed of light in vacuum
E	electric field
ϵ_0	electric permittivity in vacuum
ε	internal-energy density
F	number of freedoms
g	sum of external forces such as gravity
γ	the polytropic index; the ratio of the specific heat at constant pressure to the specific heat at constant volume
j	current density
k_B	the Boltzmann constant $1.38 \cdot 10^{-23}$ J/K
m	mass
p	plasma pressure
q	elementary charge $1.60 \cdot 10^{-19}$ C
q	net heat flux
r	position
μ_0	magnetic permeability in vacuum $4\pi \cdot 10^{-7}$ Vs/Am
ρ	mass density
ρ_q	net electrical charge density
σ_e	electrical conductivity
v	velocity
T	temperature
t	time

Stellar wind interactions

In what follows the term solar wind is used for the wind from the Sun in our solar system. The term stellar wind refers to the wind from any star (including our Sun).

2.1 The solar wind

Apart from the electromagnetic radiation that is useful in our daily life, the Sun also emits a flow of ionized plasma – the solar wind – driven by the high pressure in the solar corona. Because of the changing activity at the surface of the Sun, the properties of the solar wind display large variations. Typical values of the solar wind and how they scale with the distance from the Sun are given in Table 2.1.

The solar wind is emitted radially from the Sun, and in the ecliptic plane of the planets it is therefore a good approximation to say that the solar wind velocity only has one component u_{sw} ^{*}. What complicates the description of the solar wind is the rotation of the Sun which winds up the interplanetary magnetic field (IMF) into a rotating spiral. The Sun has a rotation period of approximately 25.4 days (near the ecliptic plane) which gives an angular rotation speed ω . In a frame that rotates with the Sun the angular component of the solar wind is not negligible. Assuming that the magnetic field is frozen into the emitted plasma, we get a relationship between the angular and radial components of the solar wind:

$$\frac{B_\varphi}{B_r} = \frac{-\omega r}{u_{sw}}. \quad (2.1)$$

For typical values at $r = 1$ AU

$$-\omega r = \frac{2\pi}{25.4 \cdot 24 \cdot 3600} \cdot 1.50 \cdot 10^{11} \approx -4.3 \cdot 10^5 \text{ m/s} \quad (2.2)$$

which gives an IMF angle of $\arctan(-\omega r/u_{sw}) = 45$ degrees relative to the radial direction.

2.2 Comets

A comet is a small solid body that at some point in its orbit displays a large atmosphere, or coma[†], of gas or dust (or both). There is a small nucleus, typically of a few kilometers, and sufficiently close ($\propto 10$ AU) to the Sun the coma starts developing. Solids of the

^{*}This neglects the angular motion of a planet which causes an aberration of a few degrees.

[†]The word coma originates from the Greek for "hair of the head" which can be a good visual description of a comet.

Table 2.1. Typical solar wind properties at Earth and its closest neighbors, adapted from [53]. R – distance away from the Sun – is given in astronomical units, $1 \text{ AU} \approx 1.5 \cdot 10^{11} \text{ m}$. Proton number density n_{sw} is noted in cm^{-3} , magnetic field magnitude in nano Tesla, proton and electron temperatures in eV ($1 \text{ eV} = 1.16 \cdot 10^4 \text{ K}$). IMF angle is the direction of the magnetic field relative to the Sun-planet direction in degrees.

Planet	R	n_{sw}	B	T_p	T_e	IMF angle
Venus	0.72	14	10	10	17	36
Earth	1.00	7	6	8	15	45
Mars	1.52	3	3	6	13	57
Scaling	-	$\frac{1}{R^2}$	$\frac{\sqrt{2R^{-2}+2}}{R}$	$\sqrt[3]{\frac{1}{R^2}}$	$\sqrt[3]{\frac{1}{R}}$	-

nucleus will then start to form gases which are photodissociated and photoionized. The outgassing will also carry along dust particles of micrometer size from rocky materials. The result is usually two distinct tails: the ion tail and the dust tail. The details of the process are complicated but we can basically see the dust tail as driven by the solar electromagnetic radiation, while the ion tail is caused by the solar wind. The dust is subject to radiation pressure, i.e. the force from solar photons, and will be driven away from the Sun at speeds which are often comparable to the orbital speed. The dust tail will thus appear curved since the radial and orbital velocity components of a dust particle will be of the approximately same orders of magnitude. The ion tail is on the other hand almost only radially directed from the Sun since the cometary ions are picked up by the Solar wind. The solar wind speed is so much larger than the cometary orbital speed, approximately 400 km/s compared to 40 km/s, which will cause the ion tail to appear straight. A typical cometary orbit and the two tails are shown in Figure 2.1. Altitude density profiles for ions and neutrals of the used cometary models are shown in Figure 2.2.

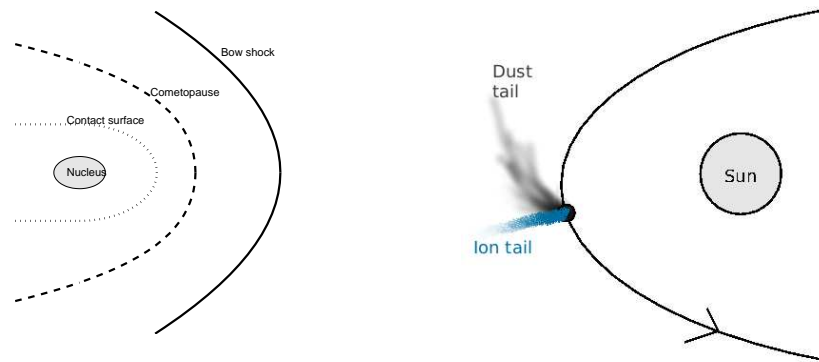


Figure 2.1. (Left) The different boundaries formed around a comet when interacting with the solar wind. (Right) The two distinct tails of a comet.

The comets in our Solar system orbit the Sun with periods ranging from a couple of years to 10 million years. Since the cometary atmospheres display large quantities of water, it is believed that comets were formed far out in the Solar system at the final stage of the formation of the Solar system. Being unable to survive close to the Sun[‡] comets are

[‡]It is not uncommon that a comet loses all of its volatiles because of the large loss rate close to the Sun. It then becomes a *dead comet* – a solid body very similar to an asteroid.

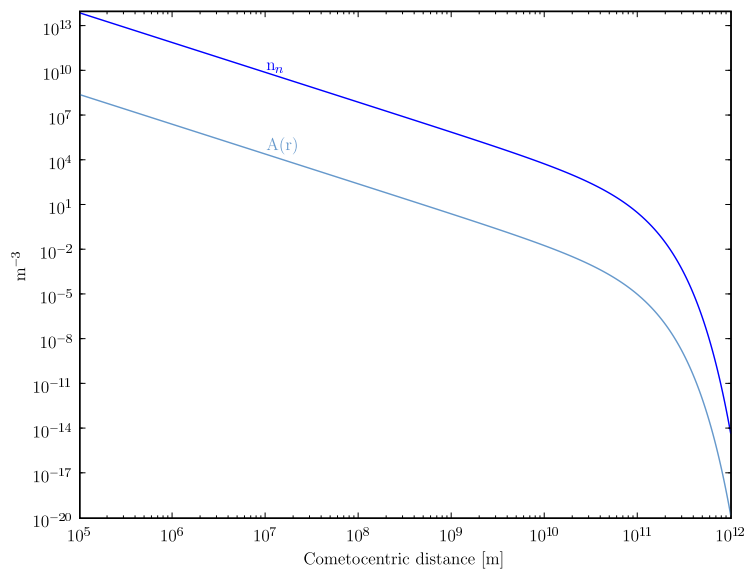


Figure 2.2. The number density m^{-3} of Halley at 0.82 AU from the Sun ($1 \text{ AU} = 1.5 \cdot 10^{11} \text{ m}$) as used in Paper III. Also shown is the production $A(r) \text{ m}^{-3}\text{s}^{-1}$ of cometary ions.

relatively unchanged since the formation of the Sun. In that way they are unique compared to the known planets and constitute a sort of time machine – a possibility to study the conditions from the time when they were formed. There are further, the more speculative, reasons for cometary studies. Some scientists argue that cometary impacts on Earth during the period of heavy bombardment $4 \cdot 10^9$ years ago could be the origin of oceans and atmospheres and therefore life itself. And, reinforced by a couple of Hollywood films, some people think we should give cometary studies high priority since it is possible that a future cometary impact could be a threat to life on Earth.

An active comet can physically be characterized by the production parameter Q which denotes the number of gas molecules produced per second. The production rate is, as explained above, highly dependent on the heliocentric distance and is therefore either stated for a comet's perihelion location (i.e. its maximum production) or for 1 AU. A'Hearn et al. [1] underline that the dependence on heliocentric distance r_H varies considerably from one comet to another, but estimate a general dependence as $Q \propto r_H^{-2.7}$. Production rates for a number of comets are shown in Table 2.2 where the production rates have been scaled to 1 AU from the Sun to facilitate a comparison of sizes.

The neutrals outgassing from an active comet are ionized mainly via photoionization, creating a huge ionosphere. Newly created ions are picked up by the magnetic field frozen in the solar wind. Due to this added mass, the plasma flow around the comet decelerates. Since the flow at large distances from the comet is unaffected by the comet, the magnetic field frozen in the flow will bend around the comet – a process known as draping, shown in Figure 2.3.

There are three major boundaries, shown in Figure 2.1, formed around an active comet. Given that the production is high enough to slow down a part of the solar wind to subsonic speed a bow shock will appear. A cometopause marks a sudden dropoff in solar

wind proton density, and inside the cometopause the cometary ions predominate [34]. Full observational evidence is lacking but indications show that the cometopause might have much in common with the magnetic pileup boundary at Mars and Venus (see Section 2.3), or that this boundary is in fact a common feature for the solar wind interaction with non-magnetized or weakly magnetized bodies [47]. The innermost boundary, the pressure-balance boundary, or contact surface, is where the thermal pressure of the expanding atmosphere equals the solar wind (thermal and magnetic) pressure.

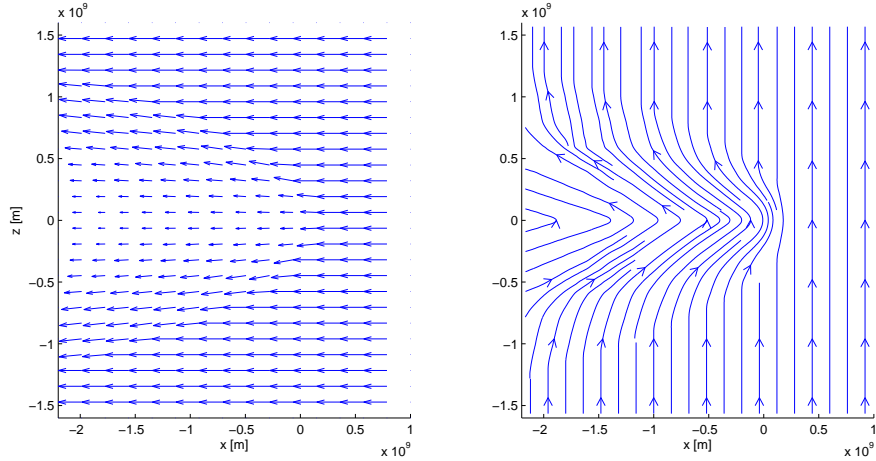


Figure 2.3. Illustration of solar wind-comet interaction in the xz -plane where the coordinate system is centered in the comet nucleus, x is towards the Sun and z along the IMF. (Left) Velocity direction and magnitude showing the deceleration of the plasma around a comet. (Right) Streamlines of the IMF, showing the draping around the comet. This is results from the simulations in Paper III.

Table 2.2. Selected comets: missions and estimated production rates at 1 AU Q_0 [s^{-1}]. Production rates are scaled from [1] as $Q_0 = Q_{ph} d_{ph}^{-2.7}$.

Comet	Spacecraft	year	Q_0
Halley	Suisei, VEGA1, VEGA2, Giotto	1986	$3 \cdot 10^{29}$
Giacobini-Zinner	ICE	1985	$5 \cdot 10^{28}$
Borrelly	Deep Space 1	2001	$5 \cdot 10^{28}$
Wild 2	Stardust	2006	$5 \cdot 10^{28}$
Tempel 1	Deep Impact	2005	$4 \cdot 10^{28}$
Churyumov-Gerasimenko	Rosetta	2014	$8 \cdot 10^{27}$
Grigg-Skjellerup	Giotto	1992	$9 \cdot 10^{26}$
Honda-Mrkos-Pajdusakova	Venus Express	2006	$8 \cdot 10^{26}$

2.3 Mars

Being similar in many aspects to Earth, Mars has for a long time attracted much scientific and non-scientific attention. For scientific purposes Mars is an important reference model and great opportunity for comparative studies to learn more about the Earth and its atmosphere.

The structure of the Martian plasma environment is shown in Figure 2.4, showing the observed bowshock and magnetic pileup boundary. With a weak intrinsic magnetic field, the Martian atmosphere interacts almost directly with the solar wind. Inside the bow shock there is the magnetosheath, inside which the magnetic pileup boundary (MPB) with a sharp dropoff in solar wind proton density marks the transition to the magnetic pileup region (MPR). The MPR is dominated by planetary ions and this is where the IMF is piled up and draped. The upper Martian atmosphere is ionized, mainly by the ultraviolet radiation from the Sun, creating a conducting ionosphere which is the effective obstacle to the solar wind. The existence of an ionopause has not yet been confirmed, but such a boundary would exist if the thermal and magnetic pressures of the created ionosphere are strong enough to balance the dynamic pressure of the solar wind [47]. A distinct difference compared to the situation at comets is the obviously much larger solid obstacle with a radius of approximately $3.4 \cdot 10^6$ m.

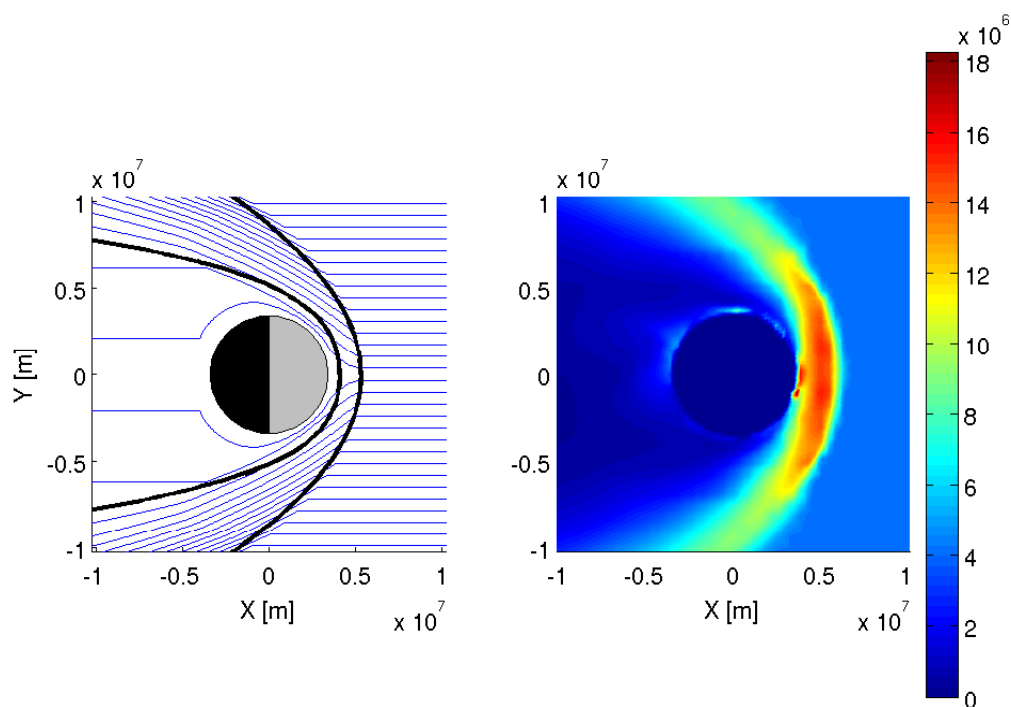


Figure 2.4. Principles of the interaction between the solar wind and Mars. The images are in the ecliptical plane with the x -axis pointing towards the Sun. (Left) Streamlines of the proton flow, adapted from [31]. Shown in thick lines are the bowshock, the magnetic pileup boundary and the Martian surface. (Right) Proton number density as obtained by [41]. These plasma simulations were used in Paper II.

Being essential for the production of energetic neutral atoms (see Section 3), the exospheric densities used for Paper II are shown in Figure 2.5.

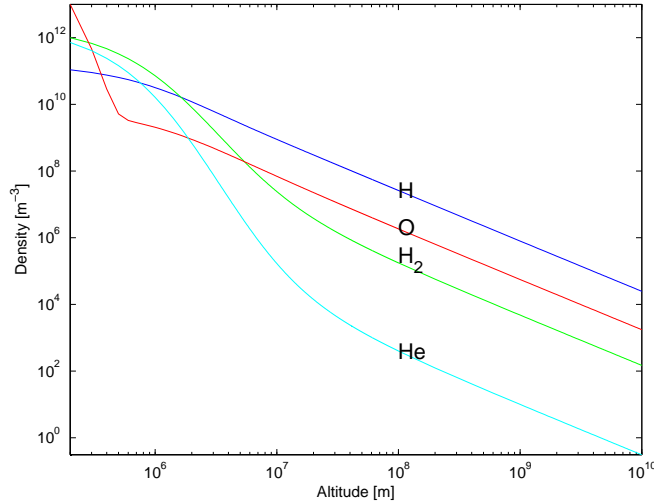


Figure 2.5. The exospheric densities of the major constituents for Mars used in Paper II. An exobase, or critical level of escape, of 200 km ($2 \cdot 10^5$ m) was used.

2.4 Exoplanets and the significance of HD 209458b

The study of extrasolar planets, or simply exoplanets, is an important means to understand the formation of our Sun and the evolution of our solar system. A more distant objective for exoplanet studies is the search for life elsewhere in the Universe.

The first confirmed detection of an exoplanet was made in 1989 [39], and the number of detected planets has since then increased rapidly. The known number of extrasolar systems is today 277 of which 25 have 2 or more planets, giving a total of 293 exoplanets [52]. Most exoplanets have been detected by the radial velocity technique, which measures the star's orbital velocity as seen from Earth. This introduces an uncertainty in the estimation of the planet's mass since the inclination of the planet's orbit with respect to the star-Earth line is unknown. The measured movement of the star is along the Earth direction, and the obtained velocity is thus $\sin(i)$ of the star's movement in its ecliptical plane.

HD 209458 is a solar-like star some 150 light years away in the constellation Pegasus with an apparent magnitude of 8[§]. HD 209458 is similar to our Sun although slightly more massive and evolved. According to conventions the first planet discovered orbiting HD 209458 was named HD 209458b. Detected in 1999 [9, 30], HD 209458b has a semi-major axis of approximately 0.045 AU. Discovery of HD 209458b was an important step in exoplanetary studies since it was the first extrasolar planet found to transit the disk of its parent star. The mass of HD 209458b could thus be measured far more exactly than any other exoplanet since the orbital inclination could be determined to 87 degrees [37]. And the radius of HD 209458b could be estimated by measuring the diminution it causes of its parent star HD 209458 during transit. Thanks to the transit detection of HD 209458b, astronomers are now also certain that the so far detected close-in, i.e. with orbits ≤ 0.05 AU, extrasolar giant planets are indeed gas giant planets, much like our own Jupiter and

[§] The apparent magnitude is a logarithmic scale for measuring the brightness of celestial bodies, where Vega is an averaged 0. This gives e.g. the following magnitudes: our Sun -27, Mars -3.0 and Uranus 5.5. The limit for observations of the naked eye under perfect conditions is at magnitude 6.5.

Saturn [11]. Physical data for HD 209458b and its parent star is summarized in Tables 2.3-2.4.

Lacking many fundamental data for the stellar system of HD 209458, an assumption of the stellar wind and its interaction with HD 209458b is that it is similar to what it would be in our solar system.

Table 2.3. Physical data for HD 209458 and comparisons to our Sun.

HD 209458	References		
Mass	$2.2 \cdot 10^{30}$ kg	$= 1.1M_{\odot}$	[37, 54]
Radius	$7.7 \cdot 10^8$ m	$= 1.1R_{\odot}$	[37, 54]
Rotation (mean)	14.4 days	$= 0.53t_{\odot}$	[43]
Effective temperature	6100 K	$= 1.1T_{eff\odot}$	[54]
Luminosity	$6.2 \cdot 10^{26}$ W	$= 1.6L_{\odot}$	[11]

Table 2.4. Physical data for HD 209458b and comparisons to Jupiter.

HD 209458b	References		
Mass	$1.2 \cdot 10^{27}$ kg	$= 0.64M_{Jup}$	[37]
Radius	$9.3 \cdot 10^7$ m	$= 1.3R_{Jup}$	[37]
Orbital period	3.52 days	$t_{Jup} = 4332$ days	[6, 43]
Semimajor axis	0.045 AU	$d_{Jup} = 5.2$ AU	[30]

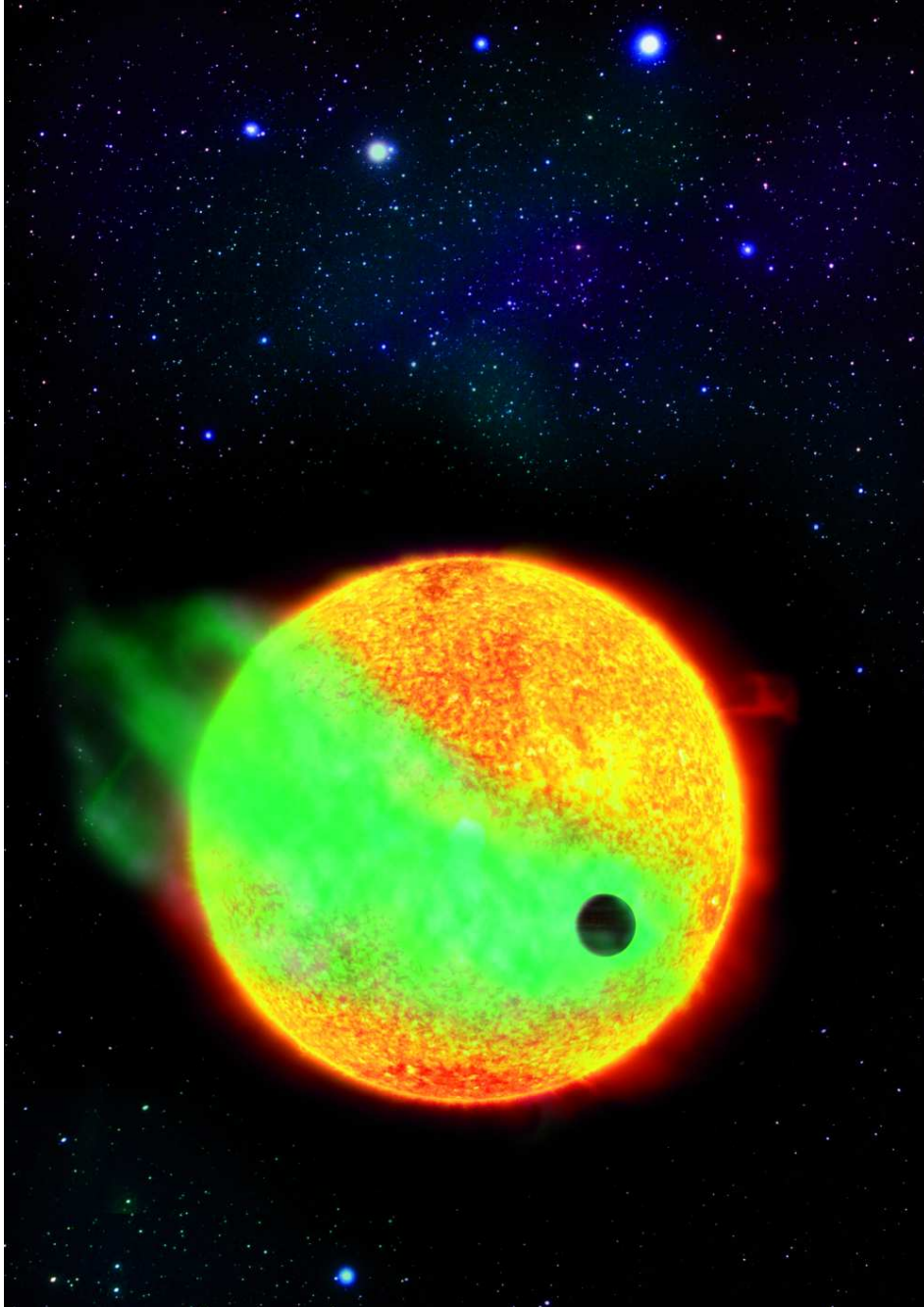


Figure 2.6. Artist's impression of HD 209458b passing (from left to right) in front of its parent star HD 209458 with a cometary shaped cloud of energetic neutral atoms (see Section 3) approximately as calculated in Paper IV. Jörgen Medman, KRAUZ & Co, NASA (JPL-Caltech, STScI.)

Energetic neutral atoms

3.1 ENA theory

ENAs from stellar wind interactions are produced wherever a stellar wind encounters a neutral atmosphere, such as found at planets and comets. Some protons in the stellar wind will come sufficiently close to neutrals for a charge-exchange reaction to take place: an electron will be transferred to the stellar wind proton turning it into a neutral. After the charge-exchange, the neutral will continue along its path with its velocity almost conserved. Being neutralized it will, however, no longer be affected by electric or magnetic fields, so the ENA will propagate in a different way than the stellar wind it originated from. The stellar wind interaction with a planetary object and the formation of an ENA is shown schematically in Figure 3.1.

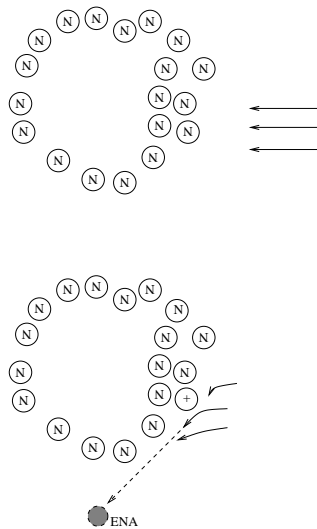


Figure 3.1. The stellar wind interaction with a planetary object. Streamlines for some protons are shown as well as how an ENA is formed.

An advantage of ENAs is that remote detecting can provide global images of stellar wind interactions. The originating direction of ENAs is certain since they travel along straight paths. ENA images can thus provide information about the stellar wind as well as the neutral atmosphere. Successful ENA detectors have thus far been used at Earth [4, 7], Mars [21], Saturn [44] and Venus [22].

3.2 Simulating ENA images

To simulate the ENA production we need models of the stellar wind flow and the neutral atmosphere. These two models together with estimations of the cross sections for the charge-exchange reaction will allow us to compute the ENA production. For a neutral density n_n of specie s , ion density n_{ion} and ion velocity u_{ion} the number of produced ENAs p per volume and second is

$$p = n_p u_p \sum_s \sigma_{cx}^s n_n^s, \quad (3.1)$$

where σ_{cx}^s is the charge-exchange cross-section for specie s . The cross sections used for Papers II & III are shown in Figure 3.2. Integrating p over a volume around an object one can obtain the total ENA production. Total ENA production has been estimated to be around 10^{25} s^{-1} at Mars and Venus [27], which seems consistent with observations [21, 22]. This corresponds to a few per cent of the solar wind flux (via obstacle effective area) at these planets. In Paper III we estimate the total ENA production from a large comet, and this production also seems to reach a few per cent of the solar wind flux.

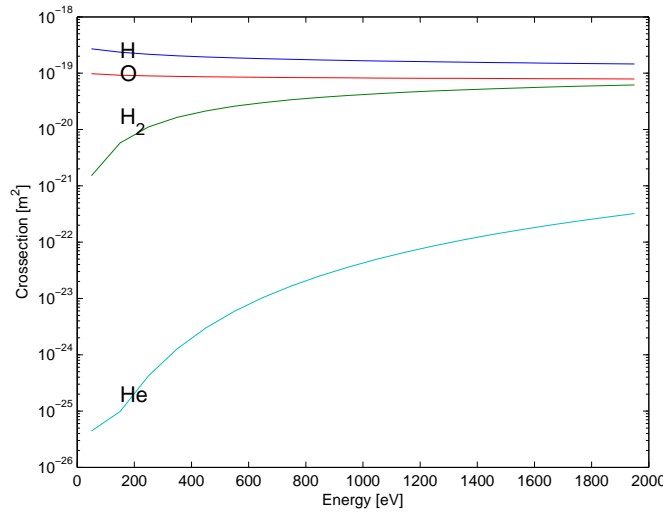


Figure 3.2. Charge-exchange cross sections with solar wind protons for constituents of martian and cometary atmospheres as used in Papers II & III. Adapted from Kallio et al [35]. $1 \text{ eV} = 1.602 \cdot 10^{-19} \text{ J}$

Since the ENA density reaches only a few per cent of the stellar wind density it is possible to estimate the ENA fluxes in a two-step simulation; first calculating the plasma flow without taking ENA production into account, and then calculating the ENA production without changing the plasma flow. This method, used in Papers II & III, will slightly overestimate the ENA production since the solar wind protons undergoing charge-exchange are not removed. A physically more correct way to simulate the ENA production is to include it self-consistently as in Papers I & IV.

No matter how the ENA production is calculated, the desired result for display is usually 2D images. Those are obtained by integrating the ENA production for directions on a 2D grid. A view direction \mathbf{d} is defined by its azimuthal direction θ and its elevation ϕ . To obtain the ENA flux for \mathbf{d} at the vantagepoint \mathbf{r} the production in the direction $-\mathbf{d}$ is cal-

culated at $\mathbf{r} + i \cdot d\mathbf{r}$ for $i = 0, 1, \dots, N$ with stepsize $d\mathbf{r}$. Doing this for a hemisphere will give the ENA flux in what resembles a fish-eye projection. The view geometry is illustrated in Figure 3.3.

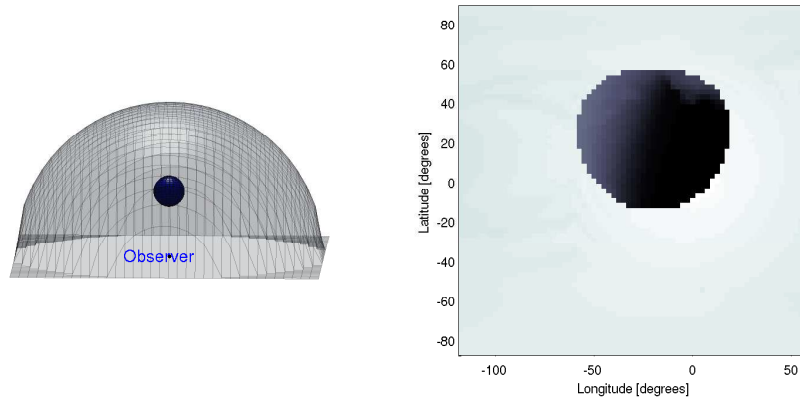


Figure 3.3. Illustration of the view geometry (with Mars in front of the Sun) for an ENA image such as in Paper II. The integration of ENA production is done over a hemisphere as shown on the left. A resulting ENA image as projected to 2D is shown on the right.

To get information about the morphology of ENA fluxes from a neutral atmosphere, images have to be produced from several vantage points. The locations of example snapshots taken by a virtual instrument are shown in Figure 3.4.

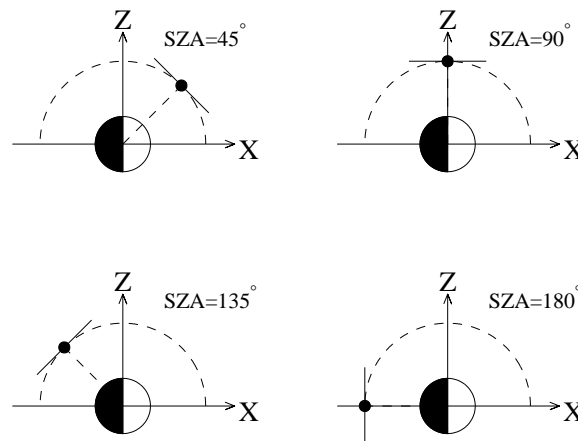


Figure 3.4. Example of vantage points for an instrument around an object. These vantage points are all in the plane perpendicular to the ecliptic plane and for different solar zenith angles.

Numerical models for space plasmas

Here I give a brief overview of the major numerical models used for space plasmas. Emphasis is on the models used in this thesis as shown in Table 4.1.

Table 4.1. Summary of models used for this thesis.

Type of numerical model	Papers
Fluid model	II, III, V
Particle model	I, IV

4.1 Fluid models

Over small spatial volumes the average properties of a collection of particles is governed by the basic conservation laws in a fluid. Since the effects of electromagnetic fields are important in space plasmas, the electromagnetic properties are added to hydrodynamics and form magnetohydrodynamic models (see below). A fluid model is computationally less costly than other models because of its more macroscopic description. Fortunately, the majority – perhaps as much as 80% – of plasma phenomena observed in space plasmas can be explained by a fluid model [10, p. 45].

4.1.1 Magnetohydrodynamic models

Magnetohydrodynamics (MHD) is the study of the motion of an electrically conducting fluid in the presence of a magnetic field. An overview can be found in [12]. What makes MHD more complex than ordinary hydrodynamics is that the conducting fluid will be affected by external fields, and at the same time its motion will modify the external fields.

MHD models consist of a simplified form of Maxwell's equations together with Ohm's law and equations of continuity for mass, motion and energy. The MHD equations can be derived from the Boltzmann equations for electron and protons, but are here given with Maxwell's equations as starting point.

4.1.2 Maxwell-Boltzmann distribution

MHD theory assumes that the particles of a plasma approximately follow the Maxwell-Boltzmann distribution function. The Maxwell-Boltzmann probability density function for a velocity component v_i has the form of a normal distribution. A normal distribution

$N(\mu, \sigma^2)$ for a random variable X with mean μ and variance σ^2 has the probability density function

$$f(X) = \frac{1}{\sigma\sqrt{2\pi}} \exp\left(-\frac{(X - \mu)^2}{2\sigma^2}\right). \quad (4.1)$$

The probability density function for the x-component of the velocity with $\sigma^2 = k_B T/m$ and $\mu = 0$ is therefore

$$f(v_x) = \sqrt{\frac{m}{2\pi k_B T}} \exp\left(-\frac{mv_x^2}{2k_B T}\right). \quad (4.2)$$

Figure 4.1 shows $f(v_x)$ for protons at different temperatures.

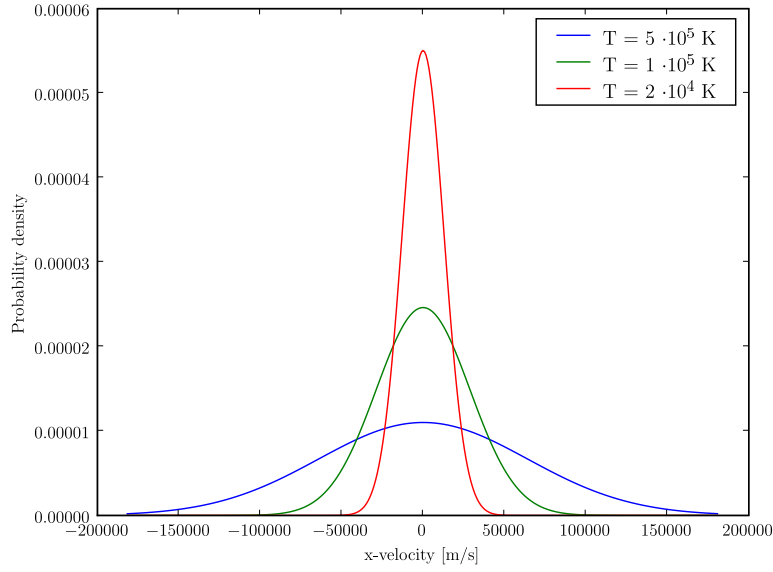


Figure 4.1. Probability density functions for protons at different temperatures. The bulk velocity is set to 0 for simplicity.

4.1.3 Maxwell's equations

The set of Poisson's equation, Ampere's law and Faraday's law together with the divergenceless of the magnetic field is usually referred to as Maxwell's equations:

$$\nabla \cdot \mathbf{E} = \frac{\rho_q}{\epsilon_0} \quad (4.3)$$

$$\nabla \times \mathbf{B} = \mu_0 \mathbf{j} + \frac{1}{c^2} \frac{\partial \mathbf{E}}{\partial t} \quad (4.4)$$

$$\frac{\partial \mathbf{B}}{\partial t} = -\nabla \times \mathbf{E} \quad (4.5)$$

$$\nabla \cdot \mathbf{B} = 0 \quad (4.6)$$

To complete the MHD model, Maxwell's equations is supplemented by the generalized Ohm's law. With the Hall current and the electron pressure gradient neglected we have

$$\sigma_e (\mathbf{E} + \mathbf{v} \times \mathbf{B}) = \mathbf{j}. \quad (4.7)$$

These equations can be simplified by a couple of assumptions. For a unit volume, the charges of the different species s cancel each other, i.e.

$$\rho_q = \sum_s q_s n_s \approx 0 \quad (4.8)$$

which is often referred to as quasi-neutrality. Further suppose the two sides of Faraday's equation (4.5) are of the same order of magnitude so that

$$\frac{E}{l_0} \approx \frac{B}{t_0} \quad (4.9)$$

for a MHD characteristic length l_0 and time t_0 . We can then neglect the high-frequency component of the electric field, arguing that

$$\frac{1}{c^2} \frac{\partial \mathbf{E}}{\partial t} \ll \mu_0 \mathbf{j} \quad (4.10)$$

since

$$\frac{\frac{1}{c^2} \left| \frac{\partial \mathbf{E}}{\partial t} \right|}{|\nabla \times \mathbf{B}|} \approx \frac{\frac{1}{c^2} \frac{E}{t_0}}{\frac{B}{l_0}} \approx \frac{1}{c^2} \frac{l_0^2}{t_0^2} = \frac{v_0^2}{c^2} \ll 1 \quad (4.11)$$

for a characteristic velocity v_0 .

4.1.4 Ideal MHD equations for the one-fluid model

In this section the commonly used one-fluid model of ideal MHD is outlined. It is applicable for a large number of the phenomena for which MHD is valid [25, p. 75].

In the simplest model of a plasma we can ignore the differences between the properties of protons and electrons and lump them together. This simplification gives a one-fluid model with a continuity equation for density

$$\frac{\partial \rho}{\partial t} + \nabla \cdot \rho \mathbf{v} = 0. \quad (4.12)$$

The continuity for momentum in a one-fluid model is given by ([36, p. 43] and [38, p. 3]):

$$\rho \frac{\partial \mathbf{v}}{\partial t} + \rho (\mathbf{v} \cdot \nabla) \mathbf{v} = -\nabla p + \mathbf{j} \times \mathbf{B} + \rho \mathbf{g}. \quad (4.13)$$

Energy conservation is in the one-fluid model preserved by [36, p. 47]:

$$\frac{\partial}{\partial t} \left(\frac{\rho v^2}{2} + \varepsilon \right) + \nabla \cdot \left[\left(\frac{\rho v^2}{2} + \varepsilon \right) \mathbf{v} + p \mathbf{v} + \mathbf{q} \right] = \mathbf{j} \cdot \mathbf{E} + \rho \mathbf{v} \cdot \mathbf{g} \quad (4.14)$$

where electromagnetic energy and externally added energy has been inserted on the right hand side. The heat flux has to be either expressed in terms of the other unknowns or we have to add new equations for the system to be solvable.

Two further assumptions must be made in order to reach ideal MHD. We neglect heat flow in the fluid [25, p. 76], i.e. assuming $\mathbf{q} \approx 0$. And the plasma must be considered as perfectly conducting [25, p. 77], i.e. that $\sigma_e \rightarrow \infty$. This is often done by approximating the plasma as collisionless[¶].

[¶]This means that $\mathbf{E} + \mathbf{v} \times \mathbf{B} = 0$ and it is when this condition is valid that it is possible to prove that the magnetic flux is frozen in to the fluid [36, p. 48]

Many MHD models use an alternative to this explicit energy conservation. Instead, it is possible to obtain an additional equation from the assumption that there is no net change in the entropy of a fluid element as it moves through the system [36, p. 47]. This can be formulated as an equation of state [38, p. 3]

$$p\rho^{-\gamma} = \text{constant} \quad (4.15)$$

where $\gamma = (F + 2)/F = 5/3$ in a three-dimensional system if the fluid is in thermodynamic equilibrium.

If we know either the pressure, the internal energy or the temperature we can derive the other quantities by the equations of state. The relations between pressure, temperature and internal energy in ideal MHD are

$$p = \frac{k_B}{m} \rho T = (\gamma - 1)\varepsilon \quad (4.16)$$

Using Ampere's law, Ohm's law and the divergenceless of \mathbf{B} we can substitute all occurrences of \mathbf{E} and \mathbf{j} (see for example [25, p76]) in Maxwell's equations (4.3)-(4.6) and include simplifications (4.8) and (4.10). We can now write 8 equations for the 8 unknowns, \mathbf{v} , \mathbf{B} , ρ and p , and form a set of ideal MHD equations for a one-fluid plasma:

$$\frac{\partial \rho}{\partial t} + \nabla \cdot \rho \mathbf{v} = 0 \quad (4.17)$$

$$\rho \frac{\partial \mathbf{v}}{\partial t} + \rho(\mathbf{v} \cdot \nabla)\mathbf{v} + \nabla \cdot \left[\left(p + \frac{B^2}{2\mu_0} \right) \mathbf{I} - \frac{\mathbf{B}\mathbf{B}}{\mu_0} \right] = \rho \mathbf{g} \quad (4.18)$$

$$\frac{\partial \mathbf{B}}{\partial t} - \nabla \times (\mathbf{v} \times \mathbf{B}) = \mathbf{0} \quad (4.19)$$

$$\frac{d}{dt} \left(\frac{p}{\rho^\gamma} \right) = 0 \quad (4.20)$$

where \mathbf{I} is a 3×3 unit matrix.

Another common MHD model of a plasma is obtained by treating the ions and electrons separately. Assuming that there is only one specie of ions, this gives a two-fluid model of the plasma. The principles are the same as for the one-fluid model, although we have to use separate continuity equations for ions and electrons. The result is a set with twice the number of equations, linked by the charge neutrality condition $Zn_i = n_e$ where Z is the ion charge number. A detailed description of a two-fluid model is for example given in [38].

4.1.5 Validity and limitations of MHD equations

In addition to the fact that MHD is only valid as a macroscopic description of a plasma, there are a number of points which limit the validity of the MHD equations:

1. A fundamental assumption for the MHD equations to be valid is that the electromagnetic variations are non-relativistic or "quasi-steady".
2. The MHD equations are derived under the assumption that the plasma retains nearly Maxwell-Boltzmann distribution functions. The equations are hence applicable for processes in which the temporal changes are slower than the slowest characteristic frequency of a single particle – i.e. the ion cyclotron frequency – and where spatial variations are smoother than the characteristic length scale of a single particle – i.e.

the ion Larmor radius [28, p. 17]. To clarify this assumption we can as an example calculate the ion cyclotron frequency (or gyrofrequency) Ω_c for typical values of the solar wind at 1 AU from the Sun (see Section 2.1). Using $B = 6$ nT, the gyrofrequency of a proton with mass m_p will be [36, p. 29]

$$\Omega_c = \frac{qB}{m_p} \approx 0.5 \text{ s}^{-1}. \quad (4.21)$$

The Larmor radius (or gyroradius) ρ_c is given by

$$\rho_c = \frac{m_p v_{\perp}}{qB} \quad (4.22)$$

where v_{\perp} is the velocity of the particle's cyclotron motion perpendicular to the magnetic field [36, p. 306]. Estimating this thermal velocity as

$$v_{\perp} = \sqrt{\frac{3k_B T_p}{m_p}} \approx 4.8 \cdot 10^4 \text{ m/s} \quad (4.23)$$

we get $\rho_c \approx 8 \cdot 10^4$ m. For such a general solar wind the MHD equations can thus be used to study phenomena with a length scale larger than $8 \cdot 10^4$ m, and where the time scales of interest are larger than 2 s ($=1/\Omega_c$).

3. We use a simplified form of Maxwell's equations where quasi-neutrality was assumed, i.e. $\rho_q \approx 0$, and where the approximation $\frac{\partial \mathbf{E}}{\partial t} \approx 0$ was used.
4. For the generalized Ohm's law we neglect the Hall current and the electron pressure gradient.
5. We assume that the gas components are not far from local thermodynamic equilibrium. We can therefore use the scalar pressure instead of the full pressure tensor [25, p. 76].
6. σ_e and μ are assumed to be uniform in the plasma. Most of the plasma properties are also assumed to be isotropic [50, p. 10].

4.2 Particle models

Perhaps the most intuitive numerical model is the particle model: a large number of particles are followed in time in their self-consistent and external electromagnetic fields. Particle models have proved capable of describing not only the collective motions but also kinetic and nonlinear effects such as plasma echoes, wave breaking and anomalous resistivity [13, p. 65]. The huge number of particles in a space plasma – typically between 10^6 m^{-3} and 10^{20} m^{-3} in the Solar System [36, p. 41] – limits the scope of particle models. Even with today's most advanced computers we have to limit the number of particles in models that are to be followed for any appreciable length of time. One particle in a model will hence be considered to represent many particles of a real plasma, or else the model can be considered to represent a very small but typical region of a plasma [14, p. 463].

The particle models in Papers I & IV use the former approach and each particle in the models are set to represent approximately 10^{33} real particles. This still results in models with a couple of millions of such meta-particles.

4.3 Kinetic theory

The variables in the fluid description of a plasma are functions of (\mathbf{r}, t) . This description is possible because we assumed (see Section 4.1.5) that the plasma has a nearly Maxwellian distribution function. The velocity distribution is therefore uniquely specified by T and \mathbf{v} (see Section 4.1.2).

If distribution functions are not Maxwellian there is a deviation from thermodynamic equilibrium [10, p. 185]. A space plasma can be far from thermal equilibrium for long periods since collisions are so rare. Fluid theory will not distinguish between two different velocity distributions $f_1(v_x)$ and $f_2(v_x)$ as long as the area under the curves are the same [10, p. 199]. The effects caused by non-equilibrium can be an important phenomena, impossible to recreate with a fluid model.

In kinetic theory a model which describes the non-equilibrium distribution of particles is included. The distribution function is in the form $f(\mathbf{r}, \mathbf{v}, t)$ which gives a description in the six-dimensional phase space. The macroscopic properties of the plasma can be then be derived from the distribution function. We get number density n and mean velocity \mathbf{v}_{mean} by moments of the distribution function:

$$n(\mathbf{r}, t) = \int f(\mathbf{r}, \mathbf{v}, t) d\mathbf{v} \quad (4.24)$$

$$\mathbf{v}_{mean}(\mathbf{r}, t) = \frac{1}{n(\mathbf{r}, t)} \int \mathbf{v} f(\mathbf{r}, \mathbf{v}, t) d\mathbf{v}. \quad (4.25)$$

The evolution of the distribution function follows the Vlasov (or collisionless Boltzmann) equation [19, p. 6]. The Vlasov equation for one specie is given by

$$\frac{\partial f}{\partial t} + \mathbf{v} \cdot \nabla f + \frac{\mathbf{F}_L}{m} \cdot \partial_{\mathbf{v}} f = 0 \quad (4.26)$$

where \mathbf{F}_L is the Lorentz force given by

$$\mathbf{F}_L = q(\mathbf{E} + \mathbf{v} \times \mathbf{B}). \quad (4.27)$$

The equations (4.24)-(4.27) together with Maxwell's equations (4.3)-(4.6) form a complete system. This alternative description of plasma can, although computationally more expensive, be more accurate for some types of plasmas. An important limitation of the kinetic model is that it assumes the plasma is collisionless.

4.4 Hybrid models

Space plasmas are characterized by a multitude of length- and time scales. In numerical modelling, one usually studies a small range of length- and time scales at a time. A hybrid, or semi-kinetic, model treats the various species of a plasma in different ways, for example as discrete particles or as fluids [58, p. 53]. By this separation, we can combine physical correctness and computational cost in various ways. For space plasmas a common type of hybrid model is when there are two kinds of species involved: electrons and ions. A successful approach within this model is to treat the electrons as a massless, charge-neutralising fluid and do particle calculations for ions [58, p. 54]. This approximation has to be consistent with the scales of the studied phenomena, which implies some condition for the model to be valid, see for example [8, p.11,072] or [58, p. 54]. Clearly, electron temporal and spatial scales must be disregarded.

High Performance Computing

5.1 Parallel computing

Floating point operations are the basis in any numerical model. Crucial to the computing time needed is therefore the number of floating point operations per second (flops) that a computer can handle. Flops can be defined as floating-point operations that operate on floating-point hardware. This definition includes floating-point additions, multiplies, comparisons and perhaps divides and square roots (depending on whether they are implemented in hardware or not). Flops figures stated for computers usually report some mix of additions and multiplications [15, p.331], and can be peak speeds or in terms of benchmark problem speeds. For rough estimations of computing time it is however usually accurate enough to count the number of basic operations that a code requires.

High performance computing usually denotes the use of supercomputers and computer clusters where the peak performane of the computer system is in or above the teraflops region. A very cost-effective way to build for large scale computing is to put commercially available processors together with interconnects. This is generally referred to as a parallel computer. The characteristics of the parallel computers used for the work presented in this thesis are listed in Table 5.1.

Table 5.1. Characteristics for the computer clusters Seth, Sarek and Milleotto used. HPC2N is the High Performance Computing Center North at Umeå University [33] and LUNARC is the Center for Scienfic and Technical computing at Lund University [40].

	Seth	Sarek	Milleotto
Computing centre	HPC2N	HPC2N	LUNARC
Number of processors	240	384	1008
Processor	AMD Athlon	AMD Opteron	Intel Xeon
Clock frequency [GHz]	1.67	2.2	3.0
Processors per node	2	2	4
Memory per node [GB]	1	8	4
Network bandwidth [Mbytes/s]	667	250	200
HP-Linpack benchmark [Gflops]	481	1330	N/A

5.1.1 CPU and wall clock times

To study the feasibility of a numerical model, total computing time, or CPU time, is often the starting point. CPU time is the sum of two parts:

user time Time spent on executing the instructions in the running program. This usually accounts for the largest part of CPU time.

system time Time spent in kernel mode on the program's behalf, i.e. requesting services from the operating system.

Wall clock time, or elapsed time, then measures actual time that has passed since execution of the program started. Wall clock time should hopefully not deviate much from CPU time but can do so if the program for example reads or writes to file a lot, or if the program requires more memory than available (and thus spends much time swapping/paging). If limited to one processor, typical simulations for Paper I would take 120 wall clock hours on Milleotto and the simulations for Paper V would take 200 wall clock hours on Seth (see Table 5.1).

Listing 5.1. Example of a parallel program in Fortran 90.

```

1 program mpiexample
2
3   include 'mpif.h'
4
5   integer numproc, rank, ierr, slicelen
6   integer, parameter :: lbound = 0, ubound = 1000
7
8   call MPI_INIT(ierr)
9   call MPI_COMM_SIZE(MPI_COMM_WORLD, numproc, ierr)
10  call MPI_COMM_RANK(MPI_COMM_WORLD, rank, ierr)
11
12  slicelen = (ubound - lbound)/numproc
13  my_lower = lbound + rank*slicelen
14
15  if ( rank == (numproc-1) ) then
16    my_upper = ubound
17  else
18    my_upper = my_lower + slicelen - 1
19  end if
20
21  write (*,10) rank, numproc, my_lower, my_upper
22
23  !! Do work on numbers <my_lower> to <my_upper>
24  !! ...
25  !! ...
26
27  call MPI_FINALIZE(ierr)
28
29 10 format ('My rank:',i3, ' of', i3, &
30  ' , interval = [', i4,',',i4,']')
31
32 end program mpiexample

```

Listing 5.2. Possible output of the example program shown in Listing 5.1.

```

1 My rank: 0 of 4, interval = [ 0, 249]
2 My rank: 1 of 4, interval = [ 250, 499]
3 My rank: 2 of 4, interval = [ 500, 749]
4 My rank: 3 of 4, interval = [ 750,1000]

```

5.1.2 Parallelization

Besides estimations of CPU and wall clock times, another important aspect of a numerical model is the benefit from parallelization. To take advantage of parallel processors the work must be divided into parts that can be distributed and calculated at individual processors. Even if we have n computers available and the computational work can be divided into n parts the computing time will seldom decrease as $1/n$. For most problems the parallelization will require overhead time and resources for communication. And for some problems another complication is that the memory might be a limitation. The benefit from parallelization for typical simulations of Papers I, III & V are shown in Figure 5.1.

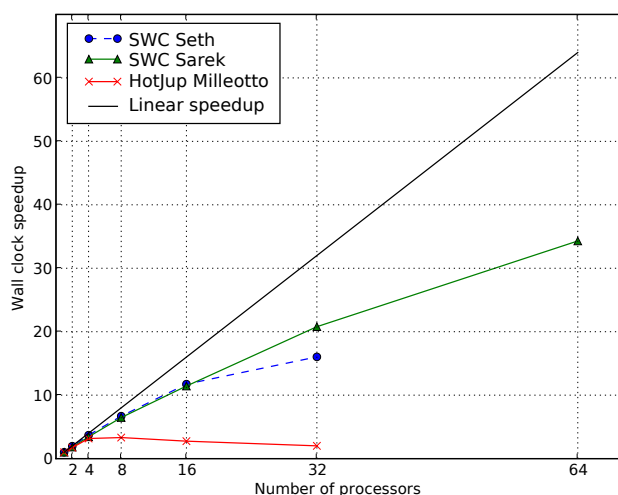


Figure 5.1. Parallelization of three sample problems. Speedup shows how much is gained from using more processors. The line of scalability shows a perfect speedup, i.e. by using n processors the speedup would be n . These sample problems were relatively small: runs on one processor for the solar wind-comet setup on Seth took approximately 2 hours, the solar wind-comet on Sarek 11 hours and the stellar wind-hot Jupiter on Milleotto 48 hours. Note that the I/O part of the simulations, i.e. writing or reading to file, is performed on a non-parallel file system and does therefore not benefit at all from parallelization. To limit the effects of sequential I/O the times were noted for runs where the I/O was set to a minimum, and I/O should account for less than 10% of the shortest computing times.

Although many problems can be divided into smaller parts, the calculations for each part can depend on global information or on results from calculations on other parts. The fundamental challenges for parallel computing are therefore how to divide the necessary computing into parts that can be computed separately, and how to communicate necessary information and results between the different processors.

Some problems are considered ideal for parallelization. An example is running the same calculations for different input, for which we separate each set of input as an independent task. A clever compiler could be able to parallelize that kind of problem so that the different tasks are calculated at different processors. Most problems are, however, not so easy to parallelize and must be parallelized manually. This includes inserting code that describes how the problem should be divided and what, to where and when to communicate between computing tasks. There are message-passing interfaces available in many programming languages that give possibilities to communicate between tasks for parallel

calculations. An example program, intended for parallel execution, is shown in Listing 5.1. Written in Fortran 90, it uses the MPI library [45] for parallelization. It shows how to slice an array into parts which are then used (only outlined) at each processor, and although simple it can serve as a skeleton for many parallelizations. The calls to MPI will make everything between Lines 8 and 27 execute on `numproc` processors. Each processor will have its own `rank` which will make `my_lower` and `my_upper` uniquely defined, and the processor will only do work on its own part of the data. Running the program on a quad-core desktop with MPICH2 [46] – a freely available implementation of MPI – might give the output shown in Listing 5.2 (the order of processors can vary).

5.2 The FLASH code

The source code of FLASH [2, 20], for which development is centered at the University of Chicago, is available upon request. Developed for astrophysical thermonuclear flashes it is mainly used for x-ray bursts and novae. The modular structure of the FLASH code does, however, permit it to be used for other purposes. Much of the work on which this thesis is based has been done using the FLASH code.

5.2.1 FLASH – structure and utilities

The modules of FLASH are mainly written in Fortran 90/95 and it uses the Message-Passing Interface (MPI) library [45] for inter-processor communication and portability. Since FLASH is intended to be a general simulation tool it is prepared so that the user can easily make his/her own setup, using the desired solvers and parts of the physics included in FLASH. Included in the source code are Python [51] scripts that will construct the setup as specified by the user. The output of FLASH is HDF5 [29] files, a versatile and portable data model. HDF5 exists for both sequential and parallel use, and the freely available library includes APIs for several programming languages. The recommended and preferred visualization tool for FLASH output is VisIt [56]. Freely available, VisIt can be used to visualize and graphically analyze the contents of various file formats. Besides the flexible user interface it is also a possible to use VisIt directly from Python scripts.

5.2.2 Parallelization in FLASH

The FLASH code divides the simulation domain spatially into blocks and distributes the blocks evenly on different processors. An advanced feature, implemented by a customized version of the PARAMESH library [49, 42], is that the calculation grid is automatically refined where (and only where) needed. In this context refinement is the process of dividing the block into smaller blocks. The refinement creates new blocks with half the length of the original, which means that in 3D a block will become 8 smaller blocks after refinement. The physical size of a block will therefore depend on its refinement level. Figure 5.2 illustrates the advantages of an adaptive calculation grid. A restriction in the refinement algorithm is that a block at maximum can only be refined one more time than its ambient blocks. If there is a need (and possibility given the setup) to refine a block further this will also therefore imply a refinement on its neighbours. A difficulty with the parallelization of an adaptive grid is that refinements (and derefinements) at a time step change the number of blocks. To keep the workload evenly distributed between processors the FLASH code regularly redistributes blocks during a simulation.

Many computations for a cell in the grid depend on the ambient cells. Each block therefore consists of a number of interior cells and *n_{guard}* of guard cells. If we have *n_{xb}* inte-

rior cells for each dimension we will then for the x -direction have interior cells at indices $1 + nguard, \dots, nguard + nxb$ and guard cells at indices $1, \dots, nguard$ and $nguard + nxb + 1, \dots, nxb + 2 \cdot nguard$. The guard cells contain boundary information needed to update the interior cells. This boundary information is usually obtained from spatially neighboring cells, but if the cell is at a boundary of the simulation domain the guard cells will contain globally specified boundary conditions.

5.2.3 FLASH experiences evaluated

I found FLASH very useful, flexible and structurally well-written. The science described in this thesis has benefitted considerably from using previously tested and optimized solvers and code utilities. Once the initial threshold for constructing a setup and understanding how to include my own modelling was overcome, it was very beneficial to work with FLASH. Apart from some manually inserted refinements the efforts spent on communication and grid handling have been minimal. The parallelization has been a small concern, and it has thus been possible to focus my efforts on formulating and inserting new models.

Although mostly robust, the Fortran 90 parts can have trouble running on certain combinations of compilers and hardware. I was for example unable to find any compiler options that would make the particle simulations for Papers I & IV run on Seth or Sarek ^{||}

The way FLASH handles refinements – rectangular blocks on a cartesian grid – can give good parallelization characteristics as seen in Figure 5.1. For some cases this will, however, limit the benefits from parallelization. As also seen in Figure 5.1, the simulations of HD 209458b actually require a longer wall clock time when running on 16 than on 8 processors. This is because for the HD 209458b setup the majority of particles, constituting the exosphere, are located in a spherical shell near the planet. Dividing this domain into 8 cartesian blocks reduces the computation time, but going further a vast majority of exospheric particles will still end up on the same processors, leaving most processors with very little workload. The drawbacks of increased communication will then for 16 processors (and more) apparently outweigh the small benefit of distributing the work for some exospheric particles. A possible workaround for an efficient parallelization of such a model would require FLASH to be able to judge when it would be beneficial to let non-neighbouring blocks be computed on the same processor.

^{||}Many combinations of compiler switches were unsuccessfully tried with the Portland group compilers 6.0-6.2. For hardware info see Table 5.1.

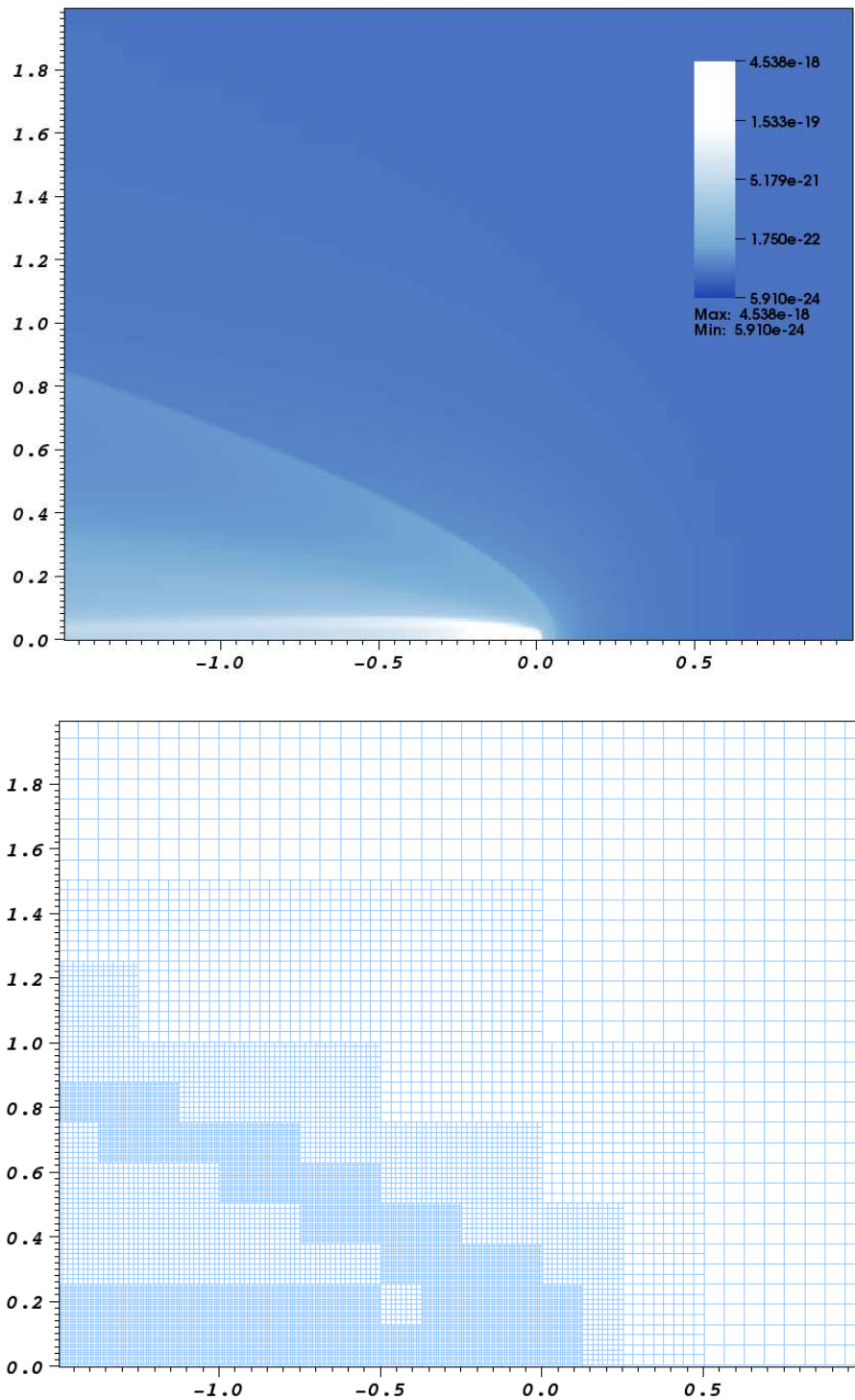


Figure 5.2. Illustration of the adaptive mesh refinement in FLASH. Above is a log₁₀ plot of the mass density around comet P45/Honda-Mrkos-Pajdusakova in the plane perpendicular to the IMF. Below is the calculation grid at the final stage that obtained the results. Using density for refinement criteria here the mesh has been refined where there are steep gradients in density. The length scale is 10^7 m.

Summary of included papers

Paper I

Energetic neutral atoms around HD 209458b: Estimations of magnetospheric properties

Observations have revealed a large population of high-velocity atomic hydrogen around HD 209458b during transit. The paper expands on an earlier work, presented in Paper IV, studying the production of ENAs as a result of the interaction between the stellar wind and the exosphere. We present an improved flow model that, together with stellar wind values similar to the ones in our solar system, further supports that the observed hot hydrogen are ENAs. We also study how the production of ENAs depends on the exospheric parameters and estimate an upper limit for the obstacle standoff distance at $(4-10) \cdot 10^8$ m. Finally we compare results obtained for the obstacle standoff distance with existing exomagnetospheric modelling, and show how the magnetic moment of HD 209458b could be determined for different exospheric scenarios.

My contributions to Paper I

I improved the flow model to include reflection at the obstacle boundary and completed the forces acting on particles. I did all numerical tests for verification and parameter studies. I wrote the majority of the paper, except for Section 2.

Paper II

The Tailward flow of energetic neutral atoms observed at Mars

The ASPERA-3 experiment on Mars Express provides the first measurements of ENAs from Mars. The purpose of ASPERA-3 is to improve our knowledge on the interaction of the solar wind with a non-magnetized planet. The paper describes the tailward ENA flow observed at the nightside of Mars. After characterizing the energy spectrum of the hydrogen ENA signals, it presents composite images of the ENA intensities and compare them to theoretical predictions (empirical and MHD models). We find that the tailward flow of hydrogen ENAs is mainly generated by shocked solar wind protons. On the other hand, no oxygen ENAs above the instrument threshold are detected. The results challenge the existing plasma models and constrain some of the exospheric densities and atmospheric loss rates at low solar activity.

My contributions to Paper II

I adapted the code used to generate ENA images to fit the observational geometry. I produced ENA images and spectra from the MHD simulations for comparison with observations.

Paper III

Energetic neutral atom imaging of comets

The paper presents the first computer simulated images of ENAs produced by charge-exchange between solar wind protons and cometary neutrals. The plasma flow is calculated with MHD simulations using the code developed for Paper V as a basis. Proton bulk flow and temperature from the MHD simulations are then used along with a model of cometary neutral densities and cross sections to calculate the production of hydrogen ENAs. The ENA production rate is integrated along lines of sight to produce images of the fluxes. We find it feasible to detect hydrogen ENAs at comets and most favorable at solar zenith angles between 80 and 130 degrees.

My contributions to Paper III

I improved the simulation tool and comet model developed in Paper V, and then adapted the model to resemble comet Halley more closely. I generalized the Matlab code that generates ENA images (previously used for Venus and Mars [27]) to work for any object and specifically for this comet. I did the final analysis and wrote the paper.

Paper IV

Energetic neutral atoms as the explanation for the high-velocity hydrogen around HD 209458b

Absorption in the stellar Lyman- α ($Ly-\alpha$) line observed during the transit of the extrasolar planet HD 209458b reveals high velocity atomic hydrogen at great distances from the planet [55][3].

In the paper we model the ENA production at HD 209458b. We show that the measured transit-associated $Ly-\alpha$ absorption could be explained by ENA production from interaction between the exosphere of HD 209458b and the stellar wind. This is the first observation of energetic neutral atoms outside the solar system. Since the stellar wind protons are the source of the observed energetic neutral atoms, this provides a completely new method of probing stellar wind conditions, and our model suggests a slow and hot stellar wind near HD 209458b at the time of the observation.

My contributions to Paper IV

I modeled the plasma flow around HD 209458b using the MHD simulation tool developed in Paper IV. This made it possible to do the first estimations of the ENA production at HD 209458b, and given the indications of high ENA production we found it worthwhile to do a more detailed study.

Paper V

MHD modeling of the interaction between the solar wind and solar system objects

We investigate the use of the general MHD solver in the FLASH code [20, 2] for the simulation of the interaction between the solar wind and solar system objects. As a test case we simulate the three-dimensional solar wind interaction with a simplified model of a comet and describe the modifications of the code. The performance of the code is studied by varying the number of processors and the number of grid cells. It is found that the code can reproduce the solar wind-comet interaction correctly and the parallelization is found satisfactory. Finally we outline how to simulate the solar wind interaction with any object using the FLASH code.

My contributions to Paper V

I developed a general FLASH module for MHD simulations of solar wind interactions. This included initial and boundary conditions corresponding to a solar wind, and a general method to insert solar system objects as source terms in the MHD solver. I adapted the existing models of solar wind-comet interaction to a formulation compatible with FLASH. I further studied the performance of the code and wrote the paper.

Bibliography

- [1] A'Hearn, M. F., Millis, R. L., Schleicher, D. G., Osip, D. J. & Birch, P. V. The ensemble properties of comets: Results from narrowband photometry of 85 comets, 1976-1992. *Icarus*, **118**, 223–270, 1995.
- [2] ASC / Alliances Center for Astrophysical Thermonuclear Flashes, 2008. URL <http://tinyurl.com/3xkdjl>.
- [3] Ben-Jaffel, L. Exoplanet HD 209458b: Inflated hydrogen atmosphere but no sign of evaporation. *Astrophysical Journal*, **671**, L61–L64, 2007.
- [4] Brandt, P. C., Barabash, S., Roelof, E. C. & Chase, C. J. Energetic neutral atom imaging at low altitudes from the Swedish microsatellite Astrid: Extraction of the equatorial ion distribution. *Journal of Geophysical Research*, **106**, 25731–25744, 2001.
- [5] Brinkfeldt, K., Gunell, H., Brandt, P., Barabash, S., Frahm, R., Winningham, J., Kallio, E., Holmström, M., Futaana, Y., Ekenbäck, A. *et al.* First ENA observations at Mars: Solar-wind ENAs on the nightside. *Icarus*, **182**, 439–447, 2006.
- [6] Brown, T. M., Charbonneau, D., Gilliland, R. L., Noyes, R. W. & Burrows, A. Hubble Space Telescope time-series photometry of the transiting planet of HD 209458. *Astrophysical Journal*, **552**, 699–709, 2001.
- [7] Burch, J. L. The first two years of IMAGE. *Space Science Reviews*, **109**, 1–24, 2003.
- [8] Chapman, S. C. & Schwartz, S. One-dimensional hybrid simulations of boundary layer processes in the AMPTE solar wind lithium releases. *Journal of Geophysical Research*, **92** (A10), 11,059–11,073, 1987.
- [9] Charbonneau, D., Brown, T. M., Latham, D. W. & Mayor, M. Detection of planetary transits across a Sun-like star. *The Astrophysical Journal*, **529**, L45–L48, 2000.
- [10] Chen, F. *Introduction to Plasma Physics*. Plenum Press, New York, USA, 1977. ISBN 0-306-30755-3.
- [11] Cody, A. M. & Sasselov, D. D. HD 209458: Physical parameters of the parent star and the transiting planet. *Astrophysical Journal*, **569**, 451–458, 2002.
- [12] Cowling, T. *Magnetohydrodynamics*. Interscience publishers, London, UK, 1957.
- [13] Dawson, J., Decyk, V., Sydora, R. & Liewer, P. High-performance computing and plasma physics. *Physics Today*, **46**, 64–70, 1993.

- [14] Dawson, J. M. & Lin, A. Particle simulation. In Galeev, A. A. & Sudan, R. N. (eds.), *Basic Plasma Physics*. Elsevier Science Publishers, Amsterdam, The Netherlands, 1989. ISBN 0-444-88020-8.
- [15] Dowd, K. & Severance, C. *High Performance Computing*. O'Reilly, Sebastopol, CA, USA, 1998.
- [16] Ekenbäck, A. & Holmström, M. MHD modeling of the interaction between the solar wind and solar system objects. In Dongarra, J., Madsen, K. & Wasniewski, J. (eds.), *Proceedings of PARA'04 State-of-the-Art*, volume 3732 of *Lecture Notes in Computer Science*, pp. 554–562. Springer-Verlag, Berlin, Germany, 2006.
- [17] Ekenbäck, A., Holmström, M., Barabash, S. & Gunell, H. Energetic neutral atom imaging of comets. *Geophysical Research Letters*, **35** (L05103), 2008.
- [18] Ekenbäck, A., Holmström, M., Selsis, F., Penz, T., Lammer, H. & Wurz, P. Energetic neutral atoms around hd 209458b : Estimations of magnetospheric properties. *Astrophysical Journal*, , 2008. Submitted.
- [19] Eliasson, B. *Numerical Simulation of Kinetic Effects in Ionospheric Plasma*. PhD thesis, Uppsala University, Sweden, 2001. ISSN 1404-5117.
- [20] Fryxell, B. *et al.* FLASH: An adaptive mesh hydrodynamics code for modeling astrophysical thermonuclear flashes. *Astrophysical Journal Suppl.*, **131**, 273, 2000.
- [21] Futaana, Y. *et al.* First ENA observations at Mars: Subsolar ENA jet. *Icarus*, **182**, 413–423, 2006.
- [22] Galli, A. *et al.* First observation of energetic neutral atoms in the Venus environment. *Planetary and Space Science*, **56**, 807–811, 2008.
- [23] Galli, A., Fok, M., Wurz, P., Barabash, S., Grigoriev, A., Futaana, Y., Holmström, M., Ekenbäck, A. *et al.* The tailward flow of energetic neutral atoms observed at Venus. *Journal of Geophysical Research*, , 2008. In press.
- [24] Galli, A., Wurz, P., Kallio, E., Ekenbäck, A. *et al.* The tailward flow of energetic neutral atoms observed at Mars. *Journal of Geophysical Research*, , 2008. Submitted.
- [25] Gombosi, T. I. *Physics of the Space Environment*. Cambridge University Press, UK, 1998. ISBN 0-521-59264-2.
- [26] Gunell, H., Brinkfeldt, K., Holmström, M., Brandt, P., Barabash, S., E.Kallio, Ekenbäck, A. *et al.* First ENA observations at Mars: Charge exchange ENAs produced in the magnetosheath. *Icarus*, **182**, 431–438, 2006.
- [27] Gunell, H., Holmström, M., Biernat, H. K. & Erkaev, N. V. Planetary ENA imaging: Venus and a comparison with Mars. *Planetary and Space Science*, **53** (4), 433–441, 2005.
- [28] Hasegawa, A. & Sato, T. *Space Plasma Physics*. Springer-Verlag, Berlin, Germany, 1989. ISBN 3-540-50411-7.
- [29] The HDF group, 2008. URL <http://tinyurl.com/69uebz>.
- [30] Henry, G. W., Marcy, G. W., Butler, R. P. & Vogt, S. S. A transiting “51 Peg-like” planet. *Astrophysical Journal*, **529**, L41–L44, 2000.

-
- [31] Holmström, M., Barabash, S. & Kallio, E. Energetic neutral atoms at Mars I : Imaging of solar wind protons. *Journal of Geophysical Research*, **107** (A10), 1277, 2002.
- [32] Holmström, M., Ekenbäck, A., Selsis, F., Penz, T., Lammer, H. & Wurz, P. Energetic neutral atoms as the explanation for the high-velocity hydrogen around HD 209458b. *Nature*, **451**, 970–972, 2008.
- [33] High Performance Computing Center North (HPC2N), 2008. URL <http://tinyurl.com/8bcjg>. Umeå university, Sweden.
- [34] Ip, W.-H. On charge exchange effect in the vicinity of the cometopause of Comet Halley. *Astrophysical Journal*, **343**, 946–952, 1989.
- [35] Kallio, E., Luhmann, J. G. & Barabash, S. Charge exchange near Mars: The solar wind absorption and energetic neutral atom production. *Journal of Geophysical Research*, **102** (A10), 22,183–22,197, 1997.
- [36] Kivelson, M. G. Physics of space plasmas. In Kivelson, M. G. & Russell, C. T. (eds.), *Introduction to Space Physics*. Cambridge University Press, Cambridge, UK, 1995. ISBN 0-521-45714-9.
- [37] Knutson, H. A., Charbonneau, D., Noyes, R. W., Brown, T. M. & Gilliland, R. L. Using stellar limb-darkening to refine the properties of HD 209458b. *Astrophysical Journal*, **655**, 564–575, 2007.
- [38] Kulsrud, R. M. MHD description of plasma. In Galeev, A. A. & Sudan, R. N. (eds.), *Basic Plasma Physics*. Elsevier Science Publishers, Amsterdam, The Netherlands, 1989. ISBN 0-444-88020-8.
- [39] Latham, D. W., Stefanik, R. P., Mazeh, T., Mayor, M. & Burki, G. The unseen companion of HD 114762 - A probable brown dwarf. *Nature*, **339**, 38–40, 1989.
- [40] Center for Scientific and Technical computing LUNARC, 2008. URL <http://tinyurl.com/6pla15>. Lund university, Sweden.
- [41] Ma, Y., Nagy, A. F., Hansen, K. C., DeZeeuw, D. L. & Gombosi, T. I. Three-dimensional multispecies MHD studies of the solar wind interaction with Mars in the presence of crustal fields. *Journal of Geophysical Research*, **107** (A10), 2002.
- [42] MacNeice, P., Olson, K., Mobarry, C., deFainchtein, R. & Packer, C. PARAMESH: A parallel adaptive mesh refinement toolkit. *Computer Physics Communications*, **126**, 330–354, 2000.
- [43] Mazeh, T. *et al.* The spectroscopic orbit of the planetary companion transiting HD 209458. *Astrophysical Journal*, **532**, L55–L58, 2000.
- [44] Mitchell, D. G., Brandt, P. C., Roelof, E. C., Dandouras, J., Krimigis, S. M. & Mauk, B. H. Energetic neutral atom emissions from Titan interaction with Saturn’s magnetosphere. *Science*, **308**, 989–992, 2005.
- [45] Message Passage Interface (MPI), 2008. URL <http://tinyurl.com/6e6ml>.
- [46] MPICH2, 2008. URL <http://tinyurl.com/6eusvj>.

- [47] Nagy, A. F., Winterhalter, D., Sauer, K., Cravens, T. E., Brecht, S., Mazelle, C., Crider, D., Kallio, E., Zakharov, A., Dubinin, E., Verigin, M., Kotova, G., Axford, W. I., Bertucci, C. & Trotignon, J. G. The plasma environment of Mars. *Space Science Reviews*, **111**, 33–114, 2004.
- [48] National Graduate School of Space Technology, 2008. URL <http://tinyurl.com/6crx8h>.
- [49] Parallel adaptive mesh refinement (PARAMESH), 2008. URL <http://tinyurl.com/3thzg5>.
- [50] Priest, E. R. Introduction to solar system MHD. In Priest, E. R. & Hood, A. W. (eds.), *Advances in Solar System Magnetohydrodynamics*. Cambridge University Press, Cambridge, UK, 1991. ISBN 0-521-40325-1.
- [51] The Python Programming Language, 2008. URL <http://tinyurl.com/7873>.
- [52] Schneider, J. The Extrasolar Planets Encyclopaedia, 2008. URL <http://tinyurl.com/5o78cw>.
- [53] Slavin, J. A. & Holzer, R. E. Solar wind flow about the terrestrial planets. I - Modeling bow shock position and shape. *Journal of Geophysical Research*, **86**, 11401–11418, 1981.
- [54] Valenti, J. A. & Fischer, D. A. Spectroscopic properties of cool stars (SPOCS). i. 1040 F, G, and K dwarfs from Keck, Lick, and AAT planet search programs. *Astrophysical Journal Supplement Series*, **159**, 141–166, 2005.
- [55] Vidal-Madjar, A., des Etangs, A. L., Désert, J.-M., Ballester, G. E., Ferlet, R., Hébrard, G. & Mayor, M. An extended upper atmosphere around the extrasolar planet HD 209458b. *Nature*, **422** (6928), 143–146, 2003.
- [56] VisIt, 2008. URL <http://tinyurl.com/3u8v6a>.
- [57] Westerberg, L. G., Vedin, J., Ekenbäck, A. & Åkerstedt, H. O. Three-dimensional flow near a reconnection site at the dayside magnetopause: Analytical solutions coupled with MHD simulations. *Journal of Plasma Physics*, **73**, 811–819, 2007.
- [58] Winske, D. Hybrid simulation codes with applications to shocks and upstream waves. *Space Science Reviews*, **42** (1-4), 53–66, 1985.

Acknowledgments

My supervisor Mats Holmström was a great source of ideas and guidance. There was always some way to proceed, a way to identify the problem or a clever workaround. Many, many thanks!

There are a number of people I also would like to thank for helping me improve the contents of this thesis. Herbert Gunell was an important link between numerical models and physics that I am grateful for. Stas Barabash remains my guru of space physics and was an invaluable resource at times. Rick McGregor did a very careful proofreading of my Änglish which improved the readability and correctness throughout this thesis.

My work was made easier by a number of other people of which there are a few I would like to thank especially. Mats Luspa, Stefan Vanhaniemi and Leif Kalla all provided the computing facilities needed in-house fast and accurately. The staff at HPC2N and LUNARC were amazingly helpful and made HPC enjoyable. Märta Syberg and Reglerteknik, KTH helped me out the last important months.

I am also deeply indebted to a lot of people who make their work and ideas available for anyone. This thesis would not have had the same quality if it wasn't for open source codes: Python, GNU/Linux, FLASH, VisIt and many, many more.

Other people might not have contributed to the thesis so much, but made the good times better and gave me strength to endure the hard times**.

My wonderful wife is vital for my wellbeing, and especially she carried our two daughters. My parents have always been a great support although never given the deserved gratitude.

Even though I highly enjoyed my work, it was important to also have fun outside of my office. The PhD students at IRF were great to hang with during coffee breaks. David McCann deserves a special thanks for the many hours we have spent sharing ups and downs. And Ellab made things happen and my poker account well filled. Playing football with Parkalompolo IK was a great pleasure thanks to all the people in and around the team. And there are a lot of other people that I have met during these years, and who have made my world more enjoyable and interesting – thank you all!

** Maybe it doesn't shine through completely, but my parallel codes and Matlab did fail unexplicably occasionally...sometimes...OK, often.

- The software used in this work was in part developed by the DOE-supported ASC / Alliance Center for Astrophysical Thermonuclear Flashes [2] at the University of Chicago.
- This research was conducted using the resources of High Performance Computing Center North (HPC2N), Umeå University [33], and the Center for Scientific and Technical Computing (LUNARC), Lund University [40].
- Andreas Ekenbäck has been a member of and was financed by the National Graduate School of Space Technology [48].